Geophysical Journal International

Geophys. J. Int. (2024) **239,** 1155–1169
Advance Access publication 2024 September 09
GJI General Geophysical Methods

https://doi.org/10.1093/gji/ggae326

Cross-gradient joint inversion and clustering of ERT and SRT data on structured meshes incorporating topography

Guido Penta de Peppo, Michele Cercato and Giorgio De Donno

"Sapienza" University of Rome, Dipartimento di Ingegneria Civile, Edile e Ambientale (DICEA), via Eudossiana 18, 00184 *Rome, Italy. E-mail: guido.pentadepeppo@uniroma1.it*

Accepted 2024 August 28. Received 2024 August 15; in original form 2024 April 17

SUMMARY

The combination of electrical resistivity and seismic refraction tomography is a common practice for the characterization of subsurface features. Presently, the cross-gradient inversion scheme stands out as one of the most robust joint approaches, and some authors modified it to manage complex topographies on unstructured meshes even if at the expense of introducing additional parameters in the inversion process. We propose in this work a cross-gradient algorithm for jointly inverting electrical and seismic tomographic data on structured meshes in cases with non-flat topography. The proposed approach preserves the benefit of the classical cross-gradient approach without the need to impose physical length scales, as for irregular meshes. The quality of the results is evaluated in comparison with independent inversion through a new standardized cross-gradient index and a fuzzy *c*-means analysis that provides an assessment of the reconstruction accuracy through the membership function. The proposed method was applied to both synthetic models and field-scale examples located in Central Italy, where an accurate geophysical reconstruction is needed for the rehabilitation of existing dams. For all cases, joint inversion yielded superior results compared to independent inversion, demonstrating better agreement with available borehole data. The effectiveness of the joint approach was also demonstrated by the post-inversion tools, where the new cross-gradient index highlighted changes in structural similarity whilst fuzzy *c*-means clustering allowed for a quantitative reconstruction (position and shape) of the main units at the sites, facilitating the detection of site layering modifications.

Key words: Joint inversion; Electrical resistivity tomography; Seismic tomography; Machine learning.

1. INTRODUCTION

Among the geophysical methods applied for civil and environmental engineering, the combined use of electrical resistivity tomography (ERT) and seismic refraction tomography (SRT) has shown to be effective for investigating the soil-structure interaction with a particular focus on the hydrogeological conditions (e.g. Bièvre *et al.* 2017), since these methods are sensitive to different physical properties of the subsurface. Electrical resistivity is a good proxy for sensing variations in water content, porosity and clay content, while seismic wave velocities are related to the elastic characteristics of materials such as density, porosity and saturation (Toksöz *et al.* 1976). Therefore, combining them in a joint inversion scheme can potentially contribute to reducing the non-uniqueness (Doetsch *et al.* 2010) thus reducing the intrinsic ambiguities in the interpretation of the inverted models (Linder *et al.* 2010).

For this reason, during the last decades joint inversions have become increasingly popular, and, consequently, many different approaches have been implemented. The structural joint inversion approach employs structural attributes as common elements between different geophysical models, without introducing any relationship between the investigated properties (Meju & Gallardo 2016). In the very first examples of structurally coupled inversion of electrical resistivity and seismic traveltime data, Zhang & Morgan (1996) and Haber & Oldenburg (1997) proposed new methods based on minimizing a measure of dissimilarity of the models in addition to the individual objective functions. In gradient-based algorithms, the direction-dependent information plays a significant role in enhancing structural features, while the magnitude of changes in the estimated parameters aids in characterizing shared boundaries (Meju & Gallardo 2016). The cross-gradient inversion introduced by Gallardo & Meju (2003) is presently one of the most robust approaches for jointly inverting ERT and SRT data as it has been applied to many real-world examples (e.g. Linde & Doetsch 2016). In this approach structural similarity between the multiple physical property distributions is achieved by imposing the constraint that the

cross-product of the gradients of the property fields should be zero at common boundaries (Gallardo & Meju 2003). Consequently, this inversion methodology can be successful where changes in the geophysical properties are aligned or the gradient is zero for one property, which is a reasonable assumption in a wide range of scenarios. Currently, there are many applications of cross-gradient joint inversion on structured meshes but only considering flat topography (e.g. Gallardo & Meju 2003, 2004, 2007; Hamdan & Vafidis 2013; Shi *et al.* 2017). For incorporating irregular tomographies, Jordi *et al.* (2020) developed a novel scheme on unstructured (triangular and tetrahedral) meshes extending the approach after Lelièvre & Farquharson (2013), which can also adapt to complex topographies. For this purpose, they modified the original cross-gradient calculation, in which the direct neighbourhood of a single cell is considered. To this end, they used all the cells lying within a pre-defined distance, at the cost of introducing an additional user-defined parameter (the radius of the selected length scale). The choice of the mesh is critical during the joint inversion particularly for ERT, where it should be sufficiently coarse to reduce the degrees of freedom and the ill-posedness of the inversion problem and limit runtime and memory occupation, while, on the other hand, the forward calculation requires a very fine grid to provide accurate results (Günther *et al.* 2006).

The impact of the coupled inversion scheme in comparison with independent inversion procedures has been classically assessed by the cross-gradient, since a reduction of this function can be seen as an improvement of the reconstruction (Meju & Gallardo 2016). Other post-inversion approaches for comparing the inverted models encompassed the use of scatterplots of inverted parameters (e.g. Linde *et al.* 2008; Doetsch *et al.* 2010), while only a few have explored the potential of machine-learning based techniques for joint and independent inversion (e.g. Hellman *et al.* 2017; Ronczka *et al.* 2017).

These works applied hard clustering algorithms as post-inversion techniques to improve joint interpretation by reducing subjective bias (e.g. Marzan *et al.* 2021), but without providing an assessment of the reliability of the performed classification, which can be achieved through soft clustering analysis. In fact, unlike crisp clustering algorithms, which assign each data point to a specific cluster, soft clustering techniques assign each point in the multidimensional space to all subsets with varying degrees of membership and can be potentially suitable for capturing the reliability of the reconstruction (Paasche *et al.* 2010). In this work, we developed a new approach for the cross-gradient joint inversion of electrical and seismic tomographic data using structured mesh in the case of not-flat topographies. The inversion algorithm, developed in Python, is based on the original cross-gradient formulation (Gallardo & Meju 2003), whose effectiveness is well demonstrated. Our approach was applied to both synthetic examples and field case studies related to geophysical investigations for rehabilitating dams. To assess the reliability of the joint inversion with respect to the classical approach and to ease the interpretation of the results, we use a new formulation of the cross-gradient function (SCG index) and a soft clustering analysis through the fuzzy *c*-means (FCM) algorithm, which served as a tool for the assessment of the reliability of the classification using the membership function.

2. METHODOLOGY

The proposed method encompassed a three-step procedure (Fig. 1): (i) first, individual inversions of ERT and SRT data are carried out through the open-source pyGIMLi package (Rücker *et al.* 2017) properly adapted to work with a newly implemented structured mesh; (ii) then, cross-gradient joint inversion is performed using the same inversion parameters, including regularization settings, initial model, and forward calculation at each inversion step and (iii) at the end of the inversion procedure, the models (individual and joint) are compared in terms of SCG and of clustered models achieved with the fuzzy *c*-means algorithm for the final interpretation. In the following sections, the procedures and algorithms used for building a structured mesh with topography, for the cross-gradient joint inversion, the computation of the SCG index and the clustering analysis are described.

2.1 Meshing

The numerical resolution of the joint formulation requires a common structured mesh to implement the cross-gradients calculation using the finite difference method. Since the pyGIMLi package (Rücker *et al.* 2017) manages not-flat topographies by unstructured meshes, where the direct neighbourhood of a single cell cannot be determined, we realized a new structured meshing algorithm able to manage even complex topographies called *FlexiMesh*. *FlexiMesh* incorporates electrode and shot/geophone points as fixed nodes of the mesh and allows the user to select the number of additional nodes placed on the surface for each sensor (1 by default). To add these additional points along the topographical surface, a linear interpolation of the given topography is carried out. The height of the cells is set equal to their width by default, but it can be customized by the user increasing with depth to compensate for the loss of resolution in ERT or changing the vertical versus horizontal ratio of the cell's dimension. This mesh (Fig. 2a) is then used during the individual and joint inversion procedures of both data sets as well as for the seismic forward computation. Conversely, for ERT data inversion a dual meshing procedure is needed for inverse and forward calculations. To this end, we derived the forward electrical mesh from the parameter grid, by adding an external region to incorporate boundary conditions (Sasaki 1989), made up of triangular elements with progressively larger dimensions to reduce the computational time (Fig. 2c). However, such mesh needs to be refined in regions with high potential gradients to limit errors (Rücker *et al.* 2006). Hence, we increased the triangle density close to the left and right borders of the parameter grid and a global refinement of the latter has been realized by bisecting cell edges, so that each quadrilateral cell is subdivided into four equal-size cells (Fig. 2d).

2.2 Cross-gradient joint inversion

Gallardo & Meju (2003) proposed a simultaneous joint inversion of electrical and seismic data for resistivity (ρ) and *P*-wave velocity (v_P) in which the cross-gradients penalty function is applied to improve the resolution of common boundaries. This dimensionless function, defining the geometrical similarity of two models as a distribution of gradients, is defined as:

$$\mathbf{t}_{\mathrm{cg}}(x, y, z) = \nabla \mathbf{m}_r(x, y, z) \times \nabla \mathbf{m}_s(x, y, z), \quad (1)$$

where $\mathbf{m}_r$ and $\mathbf{m}_s$ are the resistivity (ρ) and slowness (inverse of v_P) models, in a generic 3-D space.

An additional flexibility of the technique is that the cross-gradients constraint is also satisfied where $\nabla \mathbf{m}_r$ or $\nabla \mathbf{m}_s$ vanish, thus admitting a boundary that has a significant change only in one of the two models (Gallardo & Meju 2003). In a 2-D case, as we consider in this work, $\mathbf{t}_{\mathrm{cg}}$ always points in the strike direction and

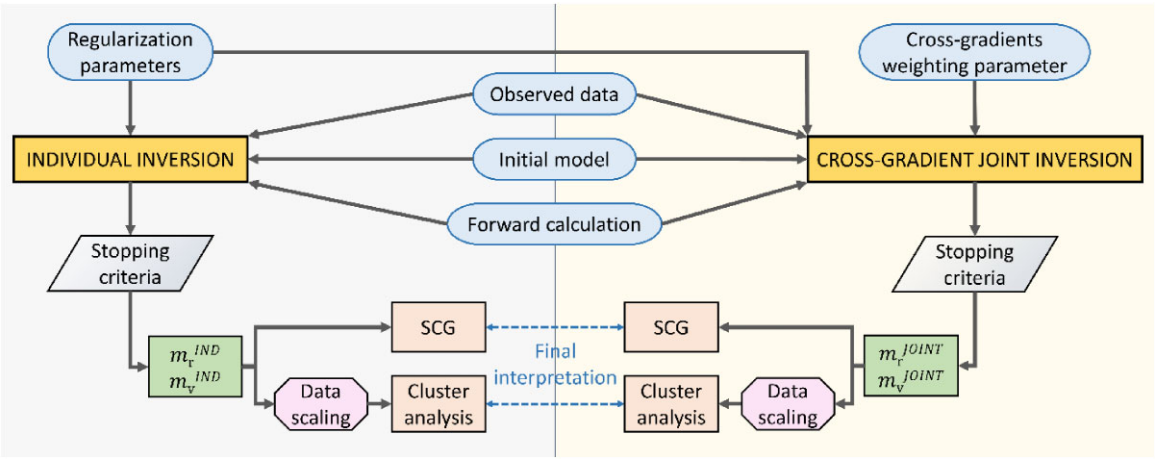

Figure 1. Flowchart of the approach used in this work.

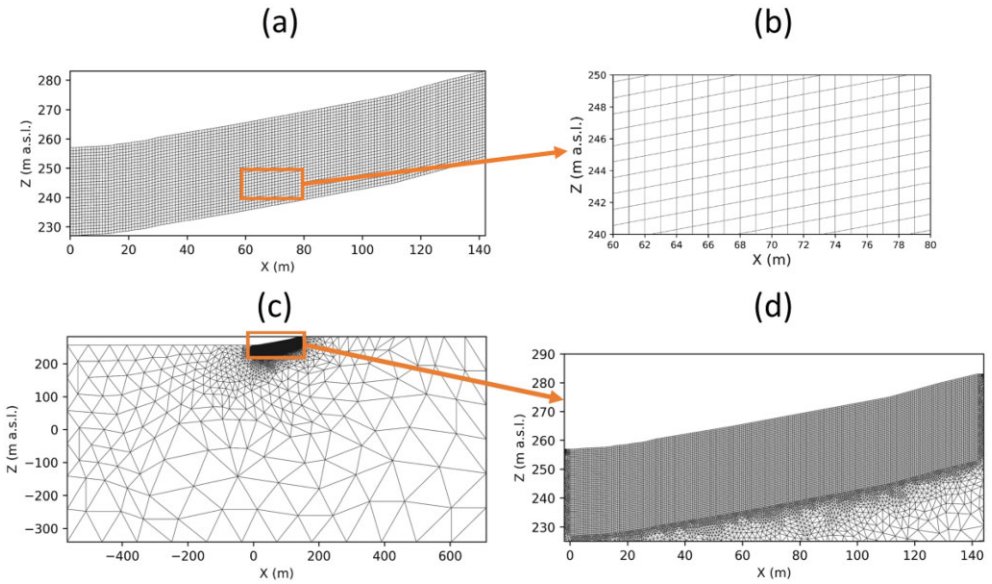

Figure 2. Meshes used during individual and joint inversions built by *FlexiMesh*: (a) mesh used for inversion of both data sets, (b) detail of its elements, (c) refined mesh for ERT forward calculation, (d) detail of the ERT forward mesh in the parametric region.

can be treated as a scalar. In this case, its y-component, referred to as t, can be calculated as:

$$t_{\mathrm{cg}}(x,z) = \left(\frac{\partial m_r(x,z)}{\partial z}\right)\left(\frac{\partial m_s(x,z)}{\partial x}\right) - \left(\frac{\partial m_r(x,z)}{\partial x}\right)\left(\frac{\partial m_s(x,z)}{\partial z}\right). \quad (2)$$

Estimating the derivatives using the forward difference method, eq. (2) can be expressed as (Gallardo & Meju 2004):

$$t_{\mathrm{cg}}(i,j) = \frac{1}{\Delta x \Delta z}\left[m_r(i,j)\left(m_s(i+1,j) - m_s(i,j+1)\right) + m_r(i,j+1)\right.$$
$$\left.\left(m_s(i,j) - m_s(i+1,j)\right) + m_r(i+1,j)\left(m_s(i,j+1) - m_s(i,j)\right)\right], \quad (3)$$

where the indices i and j define the model parameters in the x and z direction and Δx and Δz are the distances from the considered cell to the following along the two directions, referring to the centres of each cell.

The objective function of the joint inversion scheme is:

$$\Phi = \Phi_d + \lambda\Phi_m + \lambda_{\mathrm{cg}}\Phi_{\mathrm{cg}}, \quad (4)$$

in which λ and λ_{cg} are the individual and cross-gradient regularization parameters, Φ_d is the data misfit term defined as:

$$\Phi_d = \sum_{k=r,s} ||\mathbf{D}_k\left(\mathbf{d}_k - f_k\left(\mathbf{m}_k\right)\right)||_2^2, \quad (5)$$

where r and s represent resistivity and slowness, $\mathbf{D}_k$ are the data weighting matrices (since data are assumed to be uncorrelated, these matrices are diagonal and composed by the reciprocal of data errors), $\mathbf{d}_k$ the observed data and $\mathrm{f}_k(\mathbf{m}_k)$ the forward operator acting on the model $\mathbf{m}_k$.

In eq. (4) Φ_m is the regularization term not including a reference model:

$$\Phi_m = \sum_{k=r,s} ||\mathbf{C}_k\mathbf{m}_{k2}^2|| \quad (6)$$

with $\mathbf{C}_k$ the smoothness constraint matrices (Constable *et al.* 1987), regularizing the model characteristics. The cross-gradient term contains the l-2 norm of the cross-gradient penalty showed in eq. (1):

$$\Phi_{\mathrm{cg}} = ||\mathbf{t}_{\mathrm{cg}}\left(\mathbf{m}_r, \mathbf{m}_s\right)||_2^2, \quad (7)$$

The objective function is nonlinear, since resistivity and seismic forward problems, as well as the cross-gradients constraint, are nonlinear, so to minimize it we used a first-order Taylor expansion (i.e. the Gauss–Newton method) obtaining the following system formulated in terms of model perturbation:

$$\begin{bmatrix} \mathbf{DS}^p \\ \mathbf{C} \\ \sqrt{\lambda_{cg}}\mathbf{B}^p \end{bmatrix} \left[\Delta \mathbf{m}^{p+1}\right] = \begin{bmatrix} \mathbf{D}\bar{\mathbf{d}}^p \\ -\mathbf{C}\mathbf{m}^p \\ -\sqrt{\lambda_{cg}}\mathbf{t}^p \end{bmatrix}, \tag{8}$$

being p the iteration number,

$$\mathbf{D} = \begin{bmatrix} \mathbf{D}_r & 0 \\ 0 & \mathbf{D}_s \end{bmatrix}, \mathbf{S}^p = \begin{bmatrix} \mathbf{S}_r^p \\ \mathbf{S}_s^p \end{bmatrix},$$
$$\Delta \mathbf{m}^{p+1} = \begin{bmatrix} \Delta \mathbf{m}_r^{p+1} \\ \Delta \mathbf{m}_s^{p+1} \end{bmatrix}, \bar{\mathbf{d}}^p = \begin{bmatrix} \mathbf{d}_r - f_r\left(\mathbf{m}_r^p\right) \\ \\ \mathbf{d}_s - f_s\left(\mathbf{m}_s^p\right) \end{bmatrix},$$
$$\mathbf{C} = \begin{bmatrix} \sqrt{\lambda_r}\mathbf{C}_r & 0 \\ 0 & \sqrt{\lambda_s}\mathbf{C}_s \end{bmatrix}, \mathbf{m}^p = \begin{bmatrix} \mathbf{m}_r^p \\ \mathbf{m}_s^p \end{bmatrix},$$
$$\mathbf{B}^p = \begin{bmatrix} \mathbf{B}_r^p & \mathbf{B}_s^p \end{bmatrix}. \tag{9}$$

and $\mathbf{S}^p{}_r$ and $\mathbf{S}^p{}_s$ are the Jacobian or sensitivity matrices containing the partial derivatives of model responses with respect to the model parameters, whose terms are defined:

$$S_{k\,m,n}^p = \frac{\partial\left(f_k\left(\mathbf{m}_k^p\right)\right)_m}{\partial\left(m_k\right)_n} \tag{10}$$

In eqs (9) and (10), k represents the considered model (resistivity or slowness) and the subscripts m and n indicate the row and the column of the matrix element being calculated. $\mathbf{B}^p{}_r$ and $\mathbf{B}^p{}_s$ are the cross-gradient Jacobian matrices expressing the derivatives of $\mathbf{t}$ with respect to the model properties, used to approximate the cross-gradient function at the present iteration by a first-order Taylor expansion around the function at the previous iteration (Linde *et al.* 2006):

$$\mathbf{t}^{p+1} \cong \mathbf{t}^p + \mathbf{B}^p \Delta \mathbf{m}^{p+1}. \tag{11}$$

The cross-gradient sensitivity for cell m with respect to a change in model value $m_{k,n}$ is defined:

$$B_{km,n}^p = \frac{\partial\left(t_{cg}^p\right)_m}{\partial\left(m_k\right)_n} = \frac{\partial\left(\nabla \mathbf{m}_r^p \times \nabla \mathbf{m}_s^p\right)_m}{\partial\left(m_k\right)_n}. \tag{12}$$

These terms can be derived from the reduction of t in a 2-D domain shown in eq. (3), obtaining:

$$\begin{aligned}
\frac{\partial t_{cg}(i,j)}{\partial m_r(i,j)} &= \frac{1}{\Delta x \Delta z}(m_s(i+1,j) - m_s(i,j+1)), \frac{\partial t_{cg}(i,j)}{\partial m_s(i,j)} \\
&= \frac{1}{\Delta x \Delta z}(m_r(i,j+1) - m_r(i+1,j)), \\
\frac{\partial t_{cg}(i,j)}{\partial m_r(i,j+1)} &= \frac{1}{\Delta x \Delta z}(m_s(i,j) - m_s(i+1,j)), \frac{\partial t_{cg}(i,j)}{\partial m_s(i,j+1)} \\
&= \frac{1}{\Delta x \Delta z}(m_r(i+1,j) - m_r(i,j)), \\
\frac{\partial t_{cg}(i,j)}{\partial m_r(i+1,j)} &= \frac{1}{\Delta x \Delta z}(m_s(i,j+1) - m_s(i,j)), \frac{\partial t_{cg}(i,j)}{\partial m_s(i+1,j)} \\
&= \frac{1}{\Delta x \Delta z}(m_r(i,j) - m_r(i,j+1)).
\end{aligned} \tag{13}$$

We solved the system in eq. (8) using a conjugate-gradient least-squares solver (Günther *et al.* 2006), wherein an additional step of line search optimization is performed at each iteration to prevent the model from overshooting because of nonlinearity. The λ_{cg} weighting parameter was found by performing various inversions with different values and choosing the one corresponding to the lowest cross-gradient mean absolute value, as shown in Fig. 3(a). The inversion process ends when the target data misfit is reached or when no additional reduction in data misfit is obtained from one iteration to the next (Fig. 3b).

2.3 Standardized cross-gradient (SCG)

Gallardo & Meju (2004, 2007) introduced a method to assess the impact of the joint approach by visually comparing the cross-gradient (CG) values before and after the joint inversion approach, and this quantity was represented by setting a minimum and maximum threshold. Nevertheless, in many practical cases CG can fail to properly assess the impact of the coupled scheme (readers can observe such evidence concerning the cases presented in this study from Fig. S1 in Supplementary material), since this index often spans several orders of magnitude and varies from case to case, so that a consistent assessment of the benefit of the joint inversion cannot be achieved by the analysis of such parameter.

In all cases examined in this work, CG always showed a Gaussian-like distribution. For the sake of simplicity, in Fig. 4 we reported only an example of a histogram of the CG values computed for the synthetic example, where the Gaussian-like behaviour is well-visible, even though no significant differences were obtained for the other cases (readers can notice the trend of such distributions by referring to Fig. S2 in Supplementary material). Therefore, we defined a new standardized cross-gradient (SCG):

$$\mathrm{SCG} = \frac{\left|t_{cg}\right|}{\left|t_{\mathrm{CG,ind,80}}\right|}, \tag{14}$$

where $t_{\mathrm{CG,ind,80}}$ is the eightieth percentile of the cross-gradients distribution computed from individually inverted models, so that changes in the SCG after the structural inversion are solely due to the joint approach, and the previous ratio is calculated for each cell of the parameter mesh. The 80 per cent percentile was chosen after a trial-and-error procedure in which we tried also other percentiles, namely one-standard-deviation (68.2 per cent) and two-standard-deviations (95 per cent) thresholds. We selected the 80 per cent as it is able for the analysed cases to discard the tails (linked to the main anomaly) but preserve the variability of the other (minor) cross-gradient anomalies.

Low SCG values (approximating zero) indicate areas where geophysical models exhibit a high structural similarity; conversely, SCG values increase towards 1 mark areas where the models are progressively dissimilar. Values higher than 1 are related to the tails of the distribution (10 per cent on both negative and positive values), where the maximum dissimilarity is displayed. The SCG index is therefore plotted in the next sections between 0 and 10 compressing the variation between 1 and 10 to well represent any case without the need for further site-specific amendments.

2.4 Fuzzy *c*-means cluster analysis

In this paper we applied a fuzzy *c*-means (FCM) algorithm (Bezdek 1981) to both independent and joint inverted models to improve the final interpretation step. The purpose of the use of FCM is to highlight the modification made by the structural inversion to the multiparameter model, yielding quantitative integrated cross-sections that resemble both models. FCM minimizes within-cluster variances (squared Euclidean distances) through an iterative process that assigns points to clusters in a probabilistic way (Paasche *et al.*

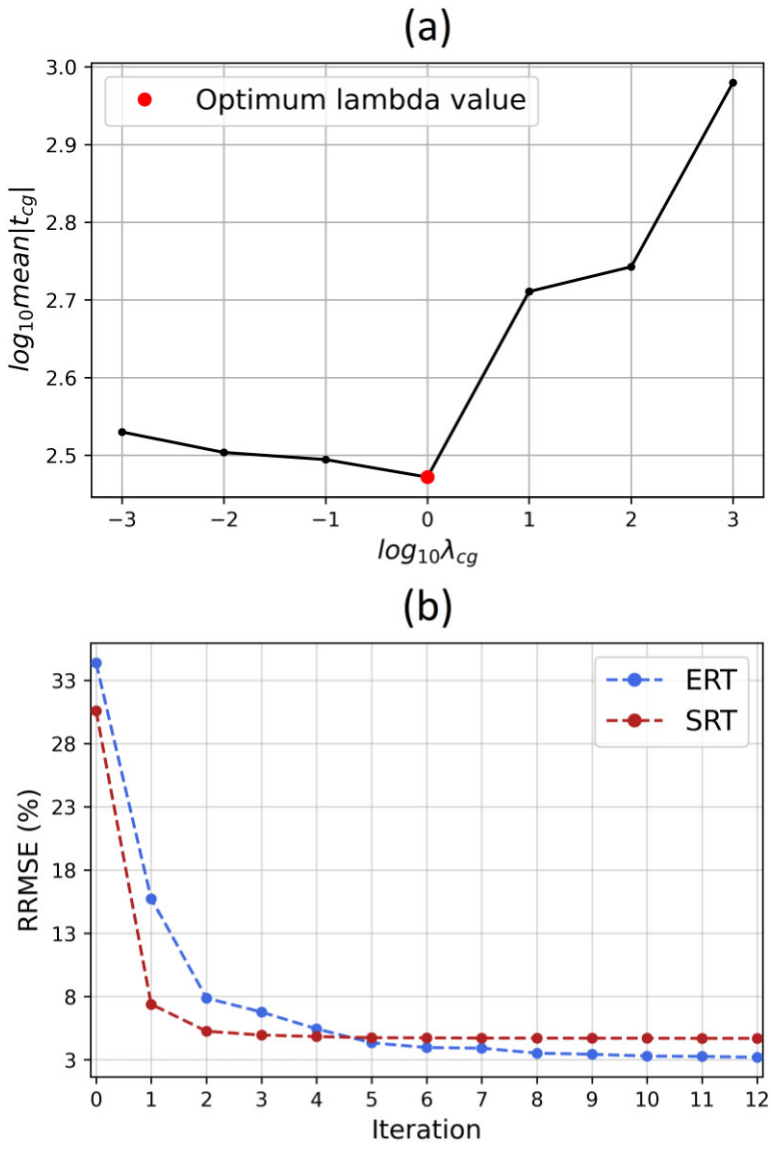

Figure 3. (a) Example of selection of the cross-gradients weighting parameter as the minimum value in the considered range $[10^{-3}–10^{3}]$, (b) related convergence curves of the data misfit for both electrical and seismic data.

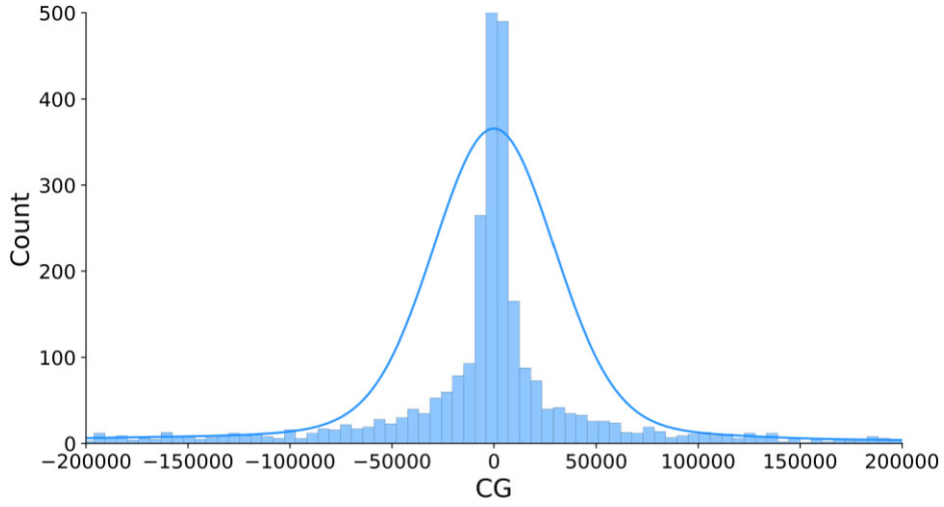

Figure 4. Example of cross-gradients distribution.

2010) reducing the objective function:

$$J = \sum_{i=1}^{c} \sum_{j=1}^{n} (u_{ij})^f ||\mathbf{d}_j - \mathbf{v}_i||_2^2, \quad (15)$$

where n is the number of data points, c the number of clusters, u_{ij} the degree of membership of data point $\mathbf{d}_j$ to cluster i defined by its centre $\mathbf{v}_i$ and the exponent f, also called the 'fuzzyfication' parameter, controls the overlap between clusters. We set this exponent as 2, which is widely accepted as a suitable choice (Paasche *et al.* 2006). Membership values are constrained to be positive by imposing the relationship:

$$\sum_{i=1}^{c} u_{ij} = 1. \quad (16)$$

After selecting the number of clusters and randomly defining their initial locations in the multiparameter space, iterative minimization yields the optimum locations of cluster centres and the distance of each data point to the centres. Data points are assigned to all clusters with partial memberships, therefore assigning each point to the cluster related to the highest membership ('defuzzyfication') makes it possible to define a single cluster with additional information about the membership. Finally, the output of fuzzy clustering is arranged in a unique plot achieved by developing the approach after Paasche *et al.* (2006), where primary colours denote different clusters while saturation is proportional to the degree of membership to the assigned cluster. In this representation, dark colours indicate membership values close to unity, whereas pale colours represent membership values near the smallest reliable one, the reciprocal of the number of clusters. Since geophysical measurements from different techniques can differ by several orders of magnitude, a preliminary logarithmic data scaling is executed to prevent one data set from dominating the distance used in clustering.

Although statistical analysis can be made for finding the optimal number of clusters where *a priori* information is not available, we set the number of clusters to be equal to the number of true layers for synthetic models and to the number of geological units detected by borehole data or from the preliminary knowledge of the site for the field case studies.

3. RESULTS

3.1 Synthetic example

The synthetic example (Fig. 5a) simulates an embankment, where a surface conductive and soft layer ($\rho = 10\ \Omega$m, $v_P = 600\ m\ s^{-1}$) overlays harder high-resistivity base ($\rho = 1000\ \Omega$m, $v_P = 1800\ m\ s^{-1}$), both lying over a lower resistivity and stiffer bedrock ($\rho = 100\ \Omega$m, $v_P = 3000\ m\ s^{-1}$). The synthetic ERT data set was generated by using 48 electrodes spaced 0.5 m apart with a dipole–dipole array having a maximum dipole length $a_{max} = 5$ and a maximum dipole separation $n_{max} = 6$. The resulting 945 apparent resistivity data points were contaminated with a zero-mean 3 per cent Gaussian error. Analogously, geophones were located for SRT at the same electrode positions, simulating one shot every two geophones. A zero-mean Gaussian noise having a 0.1 ms standard deviation (median traveltime is about 5 ms) was added to the 1128 traveltime measurements.

Results from independent inversions are shown in Fig. 5(b). The interface between superficial and intermediate layers, as well as the lateral extent of the latter are well defined in the resistivity section, while the transition from the base intermediate layer to the bedrock is not well reproduced. Structural joint inversion (Fig. 5c) highly improves the resistivity model, so that the shape of the middle anomaly is properly reconstructed. Compared to the independent model, the jointly inverted velocity model exhibits a sharper transition from the shallow (low-velocity) layer to the deeper (high-velocity) one, similar to the true model. The SCG values (Fig. 5d) from individual inversions are generally higher compared to those from the joint inversion, particularly in the deep areas close to the bottom of the model and in the transition between surface layer and bedrock (lateral zones).

Finally, cluster analysis (Fig. 6) reflects the improvement of the joint inversion procedure compared to individual inversions in terms of shape and position of the middle cluster (cluster no. 3–red). Additionally, the cross-gradient inversion yields higher membership values (more saturated tones) compared to the standard one also for the bottom layer (cluster no. 2–blue), thus demonstrating the reliability of the joint reconstruction.

3.2 Field case 1

3.2.1 Site 1: the Sterpeto dam

The embankment, located around 50 km northern of Rome (central Italy), was built to create a reservoir for irrigation and fire control (Fig. 7a). The core of the earthen dam, about 11 m high and 175 m long, is made of a quite homogeneous material, except for possible inclusion of internal drains or drainage pipes. In particular, the dam is constituted of the clayey material distributed widespread in the area, while the *in-situ* formations are Holocene sandy and marly clays superimposed to Pliocene low-permeability clays.

However, at the time of the survey, the dam was currently out of service to investigate the reasons for seepage phenomena which prevented the establishment of the originally designed working conditions.

Therefore, the geophysical survey was performed on a 166-m long profile along the crest of the dam, normally to its axis, to highlight the inner layering and the soil foundation. A string of 80 steel electrodes spaced 2 m apart was used for the ERT investigation, while the seismic survey was carried out using 8 Hz geophones with a 3-m spacing and a sledgehammer stricken vertically on a metal plate. For further details on acquisition, the reader can refer to Cardarelli *et al.* (2014). For testing the algorithm also for rough topography, we extracted the elevation profile acquired along the investigated line (Fig. 7b), without applying any filter for smoothing topographic data.

3.2.2 Site 1: results

Results from the independent inversion are shown in Fig. 8(a). In the resistivity model (Fig. 8a-left) the dam body is characterized by low resistivity values (10–13 Ωm) typical of clayey materials, except for a surface weathered zone, with a maximum thickness of about 1 m. At the sides of the dam, the resistivities are higher, indicating the presence of the alluvial deposits in the area of the embankment closure, which extends beyond the surveyed line at the right side of the section. Although deeper increases in resistivity are observed from about z = 52 m a.s.l. along the entire extent of the dam, it is not possible to clearly identify the exact position and thickness of the alluvial layer, which lacks lateral continuity, as well as the transition to the underlying Pliocene clays, in a deep low-sensitivity area. As is well known a typical issue of the isolated ERT method is a decrease

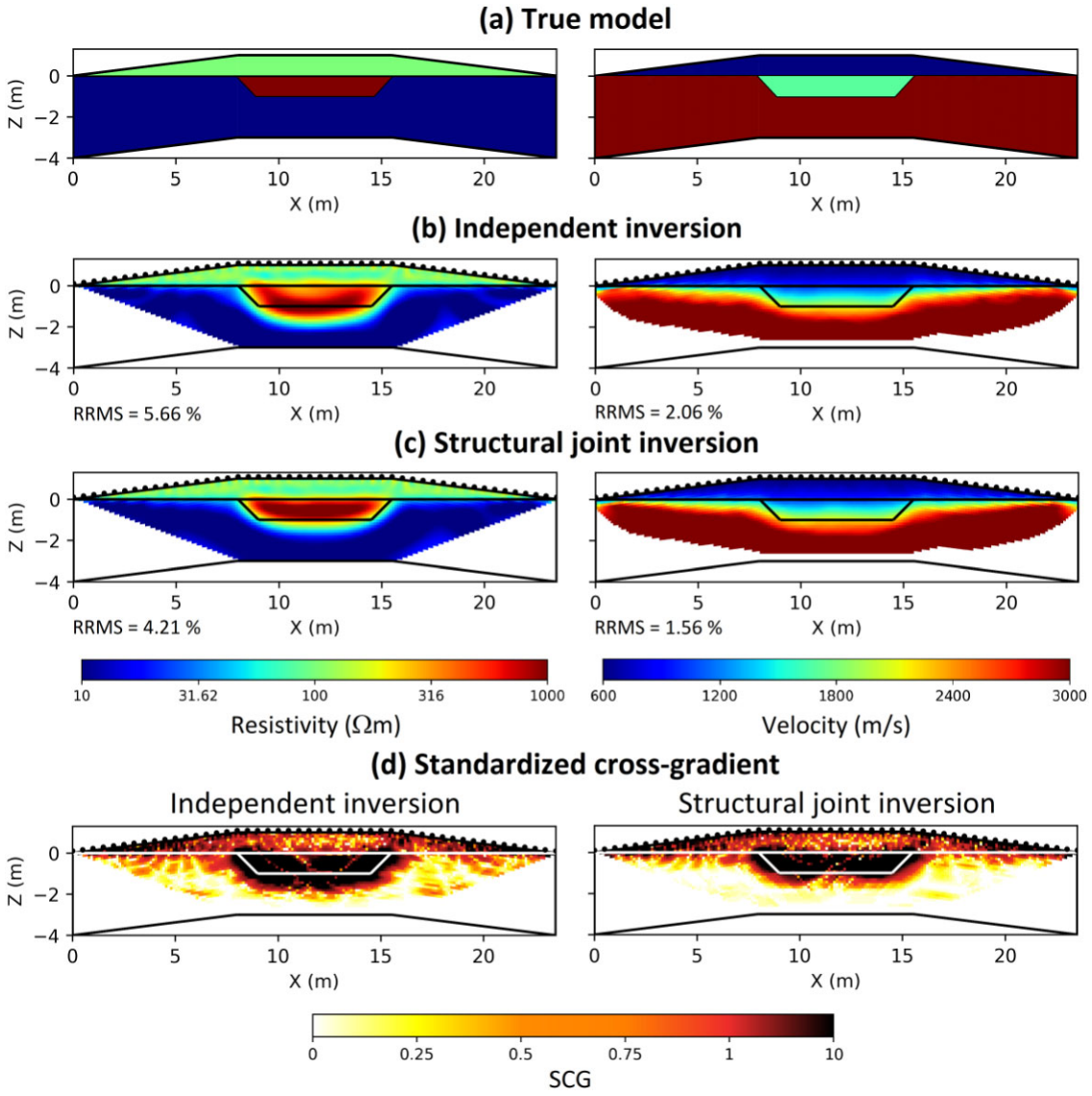

Figure 5. Synthetic example: (a) true model, (b) independent inversion, (c) cross-gradient joint inversion, (d) standardized cross-gradient. Superimposed lines indicate the true position of the interfaces.

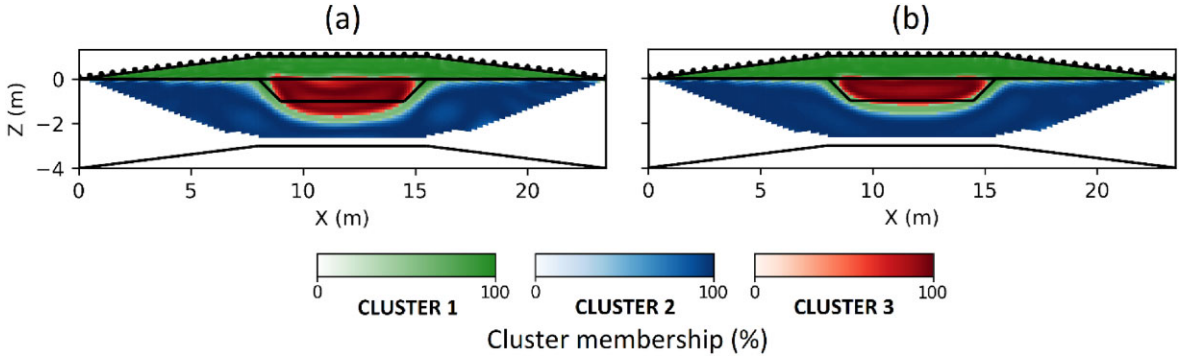

Figure 6. Synthetic example: cluster analysis. (a) Independent inversion, (b) Structural joint inversion. Superimposed lines indicate the true position of the interfaces.

in sensitivity at greater depths, which can result in lower resolution for deep sharp variations. The velocity model (Fig. 8a-right) shows the shift from the overlying low-velocity zone, including the dam body and alluvial deposits, to the underlying low-permeability clays (velocities exceeding 900 m s^{-1}), which occurs at z = 47 m a.s.l. in the central part of the line and becomes progressively shallower towards the edges of the dam. The jointly inverted resistivity model (Fig. 8b-left) remains substantially unchanged compared to

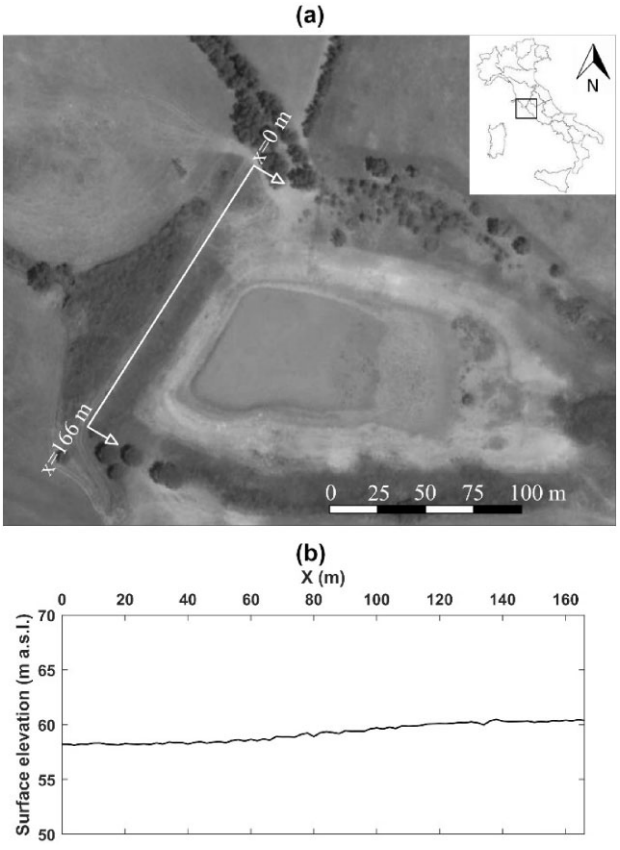

Figure 7. Site 1: (a) aerial plan of the surveyed area with location of ERT and SRT profile, (b) rough topographic profile.

the independent model in the upper part (dam body), whereas, at a depth varying between 51 and 53 m a.s.l. along the line, a continuous higher resistivity zone (ρ = 22–25 Ωm) associated with the detrital material appears. This layer is uniform in its lateral extent and characterized by a thickness between 3 and 5 m. Below this layer, at an elevation of about 48 m a.s.l., the low-resistivity underlying clay is clearly detectable. Conversely, the *P*-wave velocity model remains nearly unchanged (Fig. 8b-right). The SCG index (Fig. 8c) shows lower values for the joint approach compared to the independent one in the area below z = 53 m a.s.l. along the entire profile, where the improvement in the resistivity model is significant in the description of the detritic material and the underlying clay, as previously observed.

The integration through the fuzzy cluster analysis is presented in Fig. 9. The cross-plots in the log-10 transformed space (Figs 9a and b) show four well-separated clusters, with a more concentrated distribution of model parameters from the joint results (Fig. 9b). The high-velocity area is divided into two clusters in both reconstructions (clusters no. 3–red and no. 4–yellow), but, while clustering from the independent inversions defines these clusters with substantially overlapping velocity ranges, they are separated in terms of both resistivity and velocity values from the joint approach. The clustered section from individually inverted models (Fig. 9c) effectively describes the dam body, differentiating the surface-weathered part (cluster no. 1–green) from the almost homogeneous body (cluster no. 2–blue). However, cluster no. 3 and 4 are not able to distinguish the alluvial deposits from the underlying clays. The cross-section resulting from the joint approach (Fig. 9d) describes the dam body (clusters no. 1 and 2) similarly to the independent results, but clusters no. 3 and 4 are significantly redefined and able to distinguish the alluvial zone (cluster no. 3) from the underlying clays (cluster no. 4), with generally higher membership values (darker saturations).

3.3 Field case 2

3.3.1 Site 2: the Penne dam

The second field case study is the Penne concrete dam located in central Italy (around 130 km east of Rome) and built in the second half of the sixties as a reservoir for irrigation. The hydrogeological layout of the site consists of Pliocene marly flysch having low permeability (hydraulic conductivity $K < 10^{-6}$ m s^{-1}), covered by Holocene ancient and recent alluvial deposits of the Tavo River. The alluvium is subdivided into a fine-grained shallower unit (clay and sandy silt) and a coarse-grained high-permeable ($K > 10^{-2}$ m s−1) deeper one (sand and gravel). The dam was operating with a maximum water level well below the originally designed working conditions (256 m a.s.l.) due to seepage phenomena occurring at the right abutment, which occurred when the reservoir level was higher than 250 m a.s.l. (Cardarelli *et al.* 2018). These effects are mainly driven by the coarse-grained highly permeable alluvium and, therefore, assessing its shape, thickness, and lateral extension is pivotal for a correct design of the planned rehabilitation intervention (cut-off wall). To this end, both ERT and SRT were performed along a 142 m alignment (Fig. 10), with equally 2 m spaced sensors (electrodes and geophones). ERT profile was acquired using the IRIS Instruments Syscal Pro resistivity-metre with 48 stainless steel electrodes in a pole-dipole array configuration, while *P*-wave seismic data were recorded employing a 48-channel system of 8 Hz vertical geophones by running a shot every two geophones using an 8-gauge Minibang shotgun. Three boreholes spaced 40 m apart along the geophysical line were drilled for validating the geophysical surface investigations as shown in Fig. 10, also performing downhole tests through a 7-kg sledgehammer stricken vertically on a metal plate (*P*-wave source) and a 3-C 14 Hz borehole geophone (Geostuff), lowered progressively with a step of 1 m until reaching the bottom of the holes. Readers can refer to Cardarelli *et al.* (2018) for full results of the downhole tests.

3.3.2 Site 2: results

Results of Site 2 data inversions, shown in Figs 11(a) (individual) and 11(b) (joint), were validated by the superimposition of borehole data after Cardarelli *et al.* (2018). Geophysical models resulting from individual inversion (Fig. 11a) exhibit a three-layer geometry in generally good agreement with borehole data: low resistivity and *P*-wave velocity values (10–40 Ωm, 400–800 m s^{-1}) at shallow depths indicate the presence of fine-grained soft alluvial deposits, followed by a resistive and stiffer formation (ρ = 100–300 Ωm, v_P = 1000–1800 m s^{-1}), linked to the coarse-graded alluvium and then by a deep low-resistivity and high-velocity medium (ρ = 5–10 Ωm, v_P > 1800 m s−1) revealing the presence of the flysch unit, even if the reconstruction of this layer is strongly limited by the low sensitivity in the bottom zones. The coarse alluvium was only found in BH1 (x = 23.5 m) and BH2 (x = 63.5 m) with a thickness of 7 m (from 253 to 246 m a.s.l.) and 8 m (at the same elevation), respectively, but it was not detected in BH3 (x = 103.5 m), so we can deduce it ends between 63.5 and 103.5 m. Independent resistivity

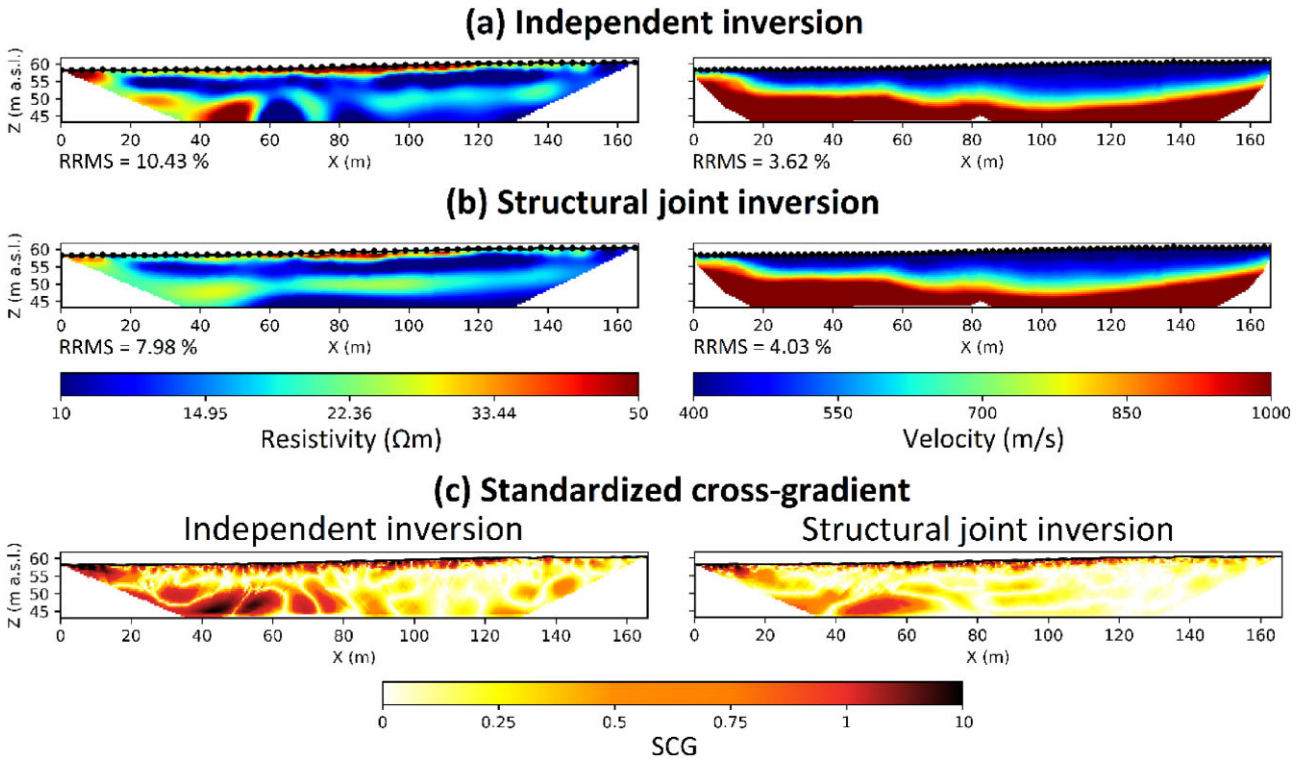

Figure 8. Site 1: (a) independent inversion, (b) cross-gradient joint inversion, (c) standardized cross-gradient.

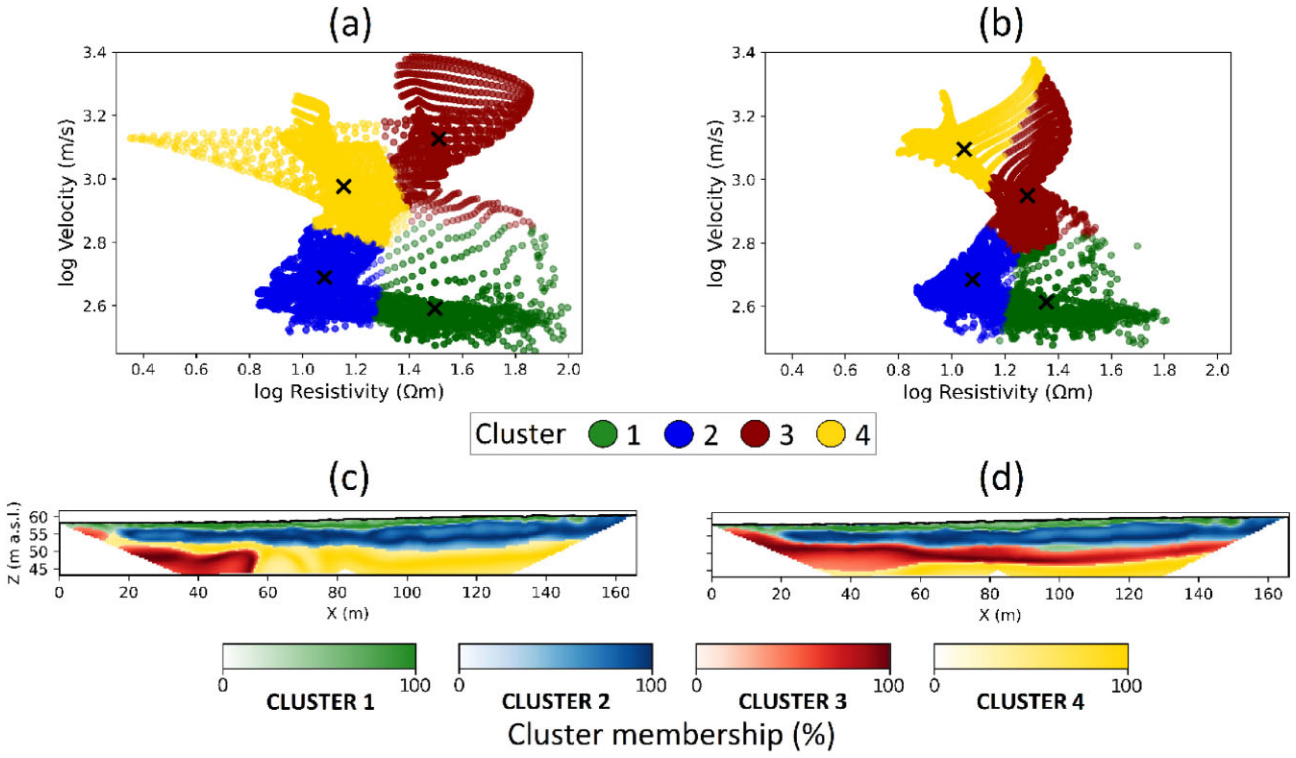

Figure 9. Site 1: (a) scatter plots of clustering results from independent inversion, (b) scatter plots of clustering results from structural joint inversion, (c) cluster analysis from independent inversion, (d) cluster analysis from structural joint inversion.

model (Fig. 11a-left) is able to reproduce the thickness of the coarse alluvium, except in the left part of the section (close to BH1), where the increased thickness is likely the result of a 3-D effect due to the proximity of the dam (see the aerial view in Fig. 10). However, its lateral extent towards BH3 ($x > 90$ m) cannot be accurately determined because of the low resolution in the bottom right part of the model (resulting from the increase in elevation) which is reflected in smoother resistivity transitions compared to the left part of the

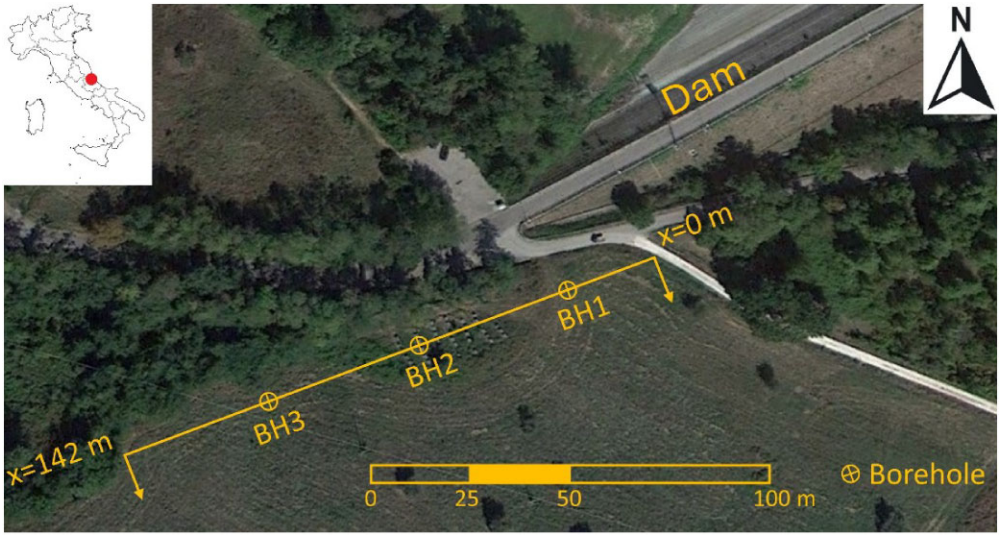

Figure 10. Site 2 at the Penne dam (Central Italy): aerial view with location of the ERT/SRT line and of the three boreholes.

section. In agreement with the results of downhole investigations, the individual *P*-wave velocity model (Fig. 11b-right) shows a progressive increase of v_P with depth in the left part, while in the right part, a low coverage area is seen around 100 m as expected due to the velocity inversion. Therefore, the depth of investigation of SRT is significantly affected by this effect and consequently, it is difficult to reconstruct the shape of the coarse-graded alluvium only through the v_P model. The jointly inverted resistivity model (Fig. 11b-left) displays a similar shape and thickness to the individual one, but its lateral extent is reduced, ending around 75–80 m in better agreement with borehole data. Conversely, the *P*-wave velocity model remains nearly unchanged (Fig. 11b-right). The SCG index (Fig. 11c) shows lower values achieved almost everywhere for the joint inversion approach compared to the independent one and a sharp decrease of SCG is seen in the middle-right part of the model ($x > 75$ m), where there is a noteworthy benefit of the coupled approach on the resistivity cross-section, as seen before.

Fig. 12 presents the quantitative integration of geophysical models through cluster analysis, in terms of cross-plots in the log-10 transformed space (Figs 12a and b) and resulting clustered sections (Figs 12c and d) for both inversion procedures. The cross-plots show that the three clusters are well separated for both methods, confirming the choice of the optimal number of clusters, with a slightly denser distribution of model parameters from joint inversion (Fig. 12b): this effect is particularly visible for clusters no. 1 and 2, suggesting a better resolution of the interfaces between these clusters (layers). The final clustered section can reconstruct the three main geological units of the study area in both cases, even though the joint approach better reconstructs the final part of the coarse alluvium unit (cluster no.3–red). In fact, it ends around $x = 85$ m, while is indeed extended towards the right boundary of the model (that is towards BH3 where the coarse-graded unit is not present) in the individual section.

3.3.3 *Site 2: A-posteriori synthetic simulation*

To further validate our results we performed *a-posteriori* synthetic simulation, choosing stratigraphy and geophysical parameters in agreement with both inverted models and borehole data. Therefore, we defined a three-layer resistivity model (Fig. 13a), which recalled the shape and the values of the inverted one (Fig. 11): a shallow unit simulating the fine-graded alluvium ($\rho = 30\,\Omega$m) is followed by a high-resistivity sand and gravel medium ($\rho = 200\,\Omega$m) with a thickness of 7 m, which becomes thinner from about $x = 75$ m until vanishing at $x = 83.5$ m, both lying over a conductive layer representing the marly flysch ($\rho = 5\,\Omega$m).

The *P*-wave velocity model is derived from both inverted model and downhole investigations, where five layers were detected. Velocities of the deeper layers (sand/gravel and flysch) are 1700 and 2400 m s^{-1}, respectively, while the fine-graded unit is sub-divided into three zones with v_P equal to 426, 750 and 1424 m s^{-1}. Measurements were generated by using the same configurations employed for field data acquisition, and additional zero-mean Gaussian noise was added as 3 per cent for apparent resistivities and 1 ms for traveltimes.

The results of individual inversions (Fig. 13b) show a good reconstruction of the shallow units and the vertical transition to the middle layer simulating the coarse alluvium at a depth of 256 a.s.l. However, the lateral extent of this unit is not correctly detected by independent inversion, as it extends horizontally well beyond its actual position for ERT, due to the lack of resolution close to the bottom of the model, and it is not well reconstructed by SRT. The latter effect is mostly due to the velocity inversion displayed in the right part of the model which prevents a good ray coverage, thus, affecting the depth of investigation in the deeper zones. Coupled models (Fig. 13c) demonstrate an improvement in the resolution of the geophysical target (coarse alluvium), particularly for ERT reconstruction. In fact, in the resistivity model this layer ends around $x = 75$–80 m consistent with its true position, while a slight benefit arising from the joint inversion is also visible in the velocity model in terms of the shape of the final part of the high-velocity layer (around $x = 75$–80 m), which better resembles the true target, and in the reconstruction of the velocity values ($v_P \sim 1400$ m s^{-1}) of the right part of the model ($x > 100$ m) which better correspond to the true ones. The comparison of SCG sections from individual and jointly inverted models (Fig. 13d) reflects the improvement of the coupled approach, exhibiting an overall decrease of the cross-gradient values with a drastic reduction in the deep zones of the cross-sections ($x > 83$ m), where the benefit the joint approach is significant.

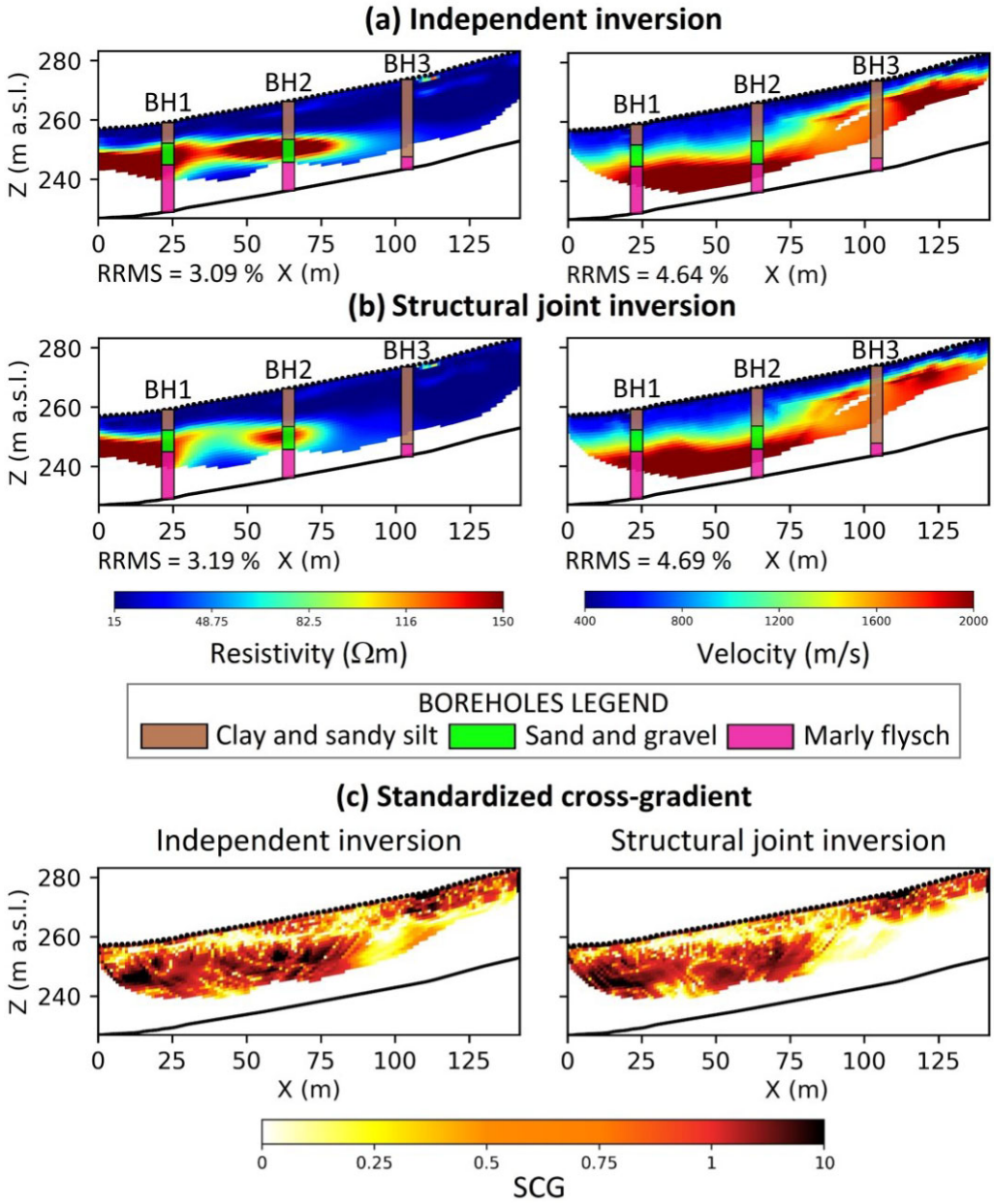

Figure 11. Site 2: (a) independent inversion, (b) cross-gradient joint inversion, (c) standardized cross-gradient.

The integrated cross-sections resulting from the cluster analysis (Fig. 14) performed by fixing the number of clusters equal to 3, that is the number of simulated geological units (fine alluvium, coarse alluvium, flysch), confirm the added value of the joint inversion approach mainly on the bottom layers (clusters no. 2 and 3). In fact, cluster 3 (coarse alluvium) is extended to the end of the section using individually inverted models (Fig. 14a), while it sharply ends around x = 80 m for the joint inversion approach (Fig. 14b) according to its true position. As an additional benefit of joint inversion the membership values in the bottom-right part of the joint clustered section are higher (darker tones), thus indicating increased confidence in the reconstruction.

4. DISCUSSION

This work is focused on the study of the enhanced accuracy in the detection of geophysical targets that can be guaranteed through a structural joint cross-gradient inversion incorporating topography. The need for a joint inversion approach (at the expense of an increasing computational effort) can be justified for complex geological or anthropogenic scenarios, where high accuracy in the detection of the different layers is required to improve the cost-effectiveness of the project. The independent inversions surely provided the main information about the layering at the two study sites, though being ineffective for reconstructing accurately the shape and position of the dam foundation (Site 1) and the high-permeability sand/gravel layer (Site 2). Both the synthetic example and the field cases demonstrated that the benefit of the joint approach is particularly significant for the low-sensitivity areas and/or where resistivity or velocity exhibit sharp transitions at great depths (Figs 5 and 8) or for low-velocity zones embedded between higher velocities layers (velocity inversion), with a significant reduction in seismic ray density (Figs 11 and 13). These results are in agreement with previous works where structural joint inversion mainly affected the low-sensitivity areas of

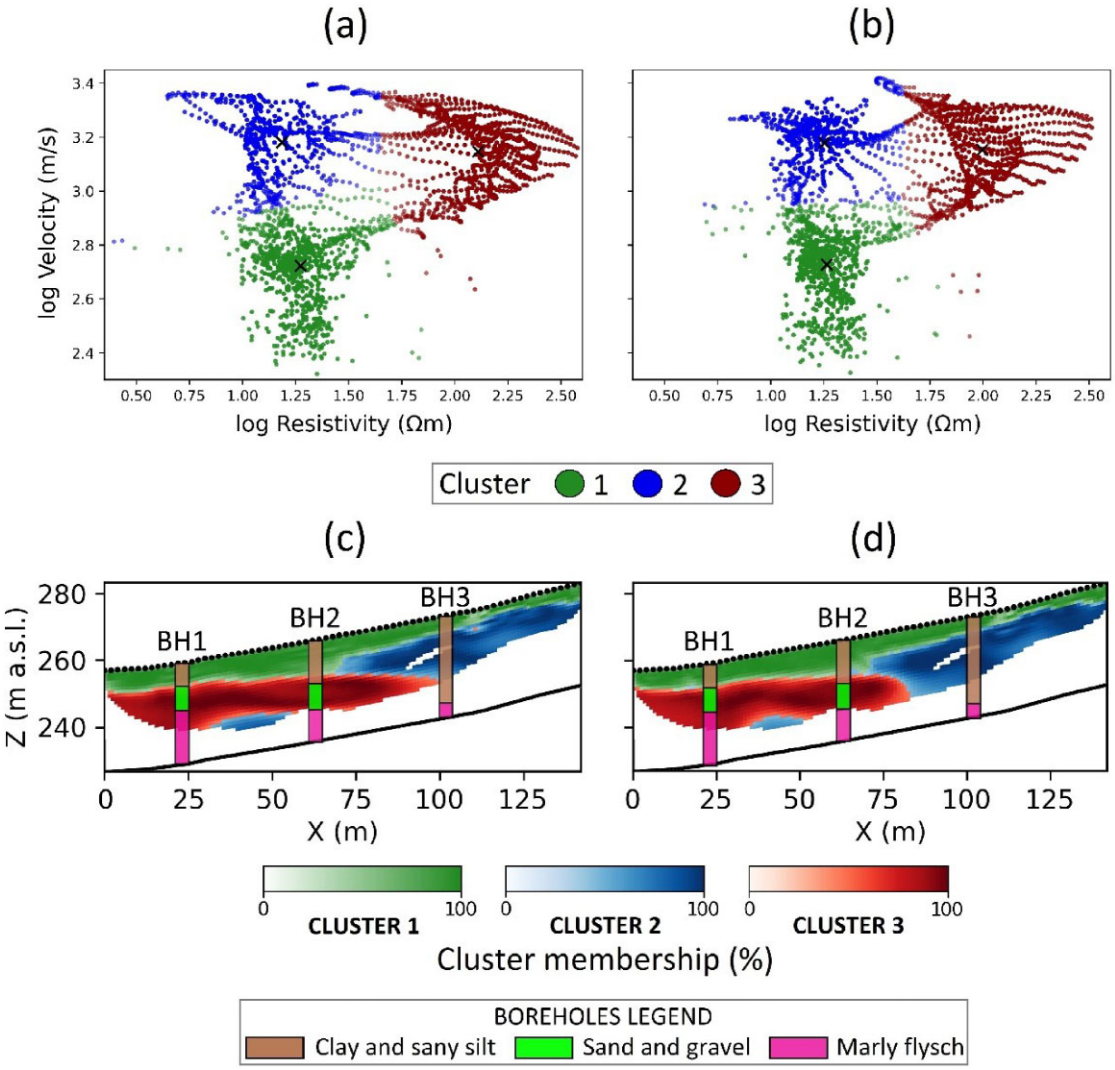

Figure 12. Site 2: (a) scatter plots of clustering results from individual inversion, (b) scatter plots of clustering results from structural joint inversion, (c) cluster analysis from independent inversion, (d) cluster analysis from structural joint inversion.

one technique through the assistance of the other, thereby obtaining more reliable models (e.g. Yari *et al.* 2021).

In recent years, some authors modified the original cross-gradient joint inversion scheme to adapt it to unstructured meshes capable of handling complex topographies (e.g. Jordi *et al.* 2020) using triangular or tetrahedral elements. Compared to these studies, which introduced a user-defined length scale parameter to compute cross-gradients and their sensitivity matrix, we preferred to adapt the original formulation (Gallardo & Meju 2003) for complex topography. This approach introduces only one additional parameter (the cross-gradients weighting parameter), which can be estimated by achieving the minimum of the mean absolute cross-gradient. Our choice is also motivated by the fact that increasing the number of unknown parameters can accentuate the ill-posedness of the inverse problem by expanding the set of admissible models, potentially leading to improper convergence of the whole inversion process. In any case, independent inversion should be always performed in advance to ensure that models are not excessively different, which might indicate that they are not structurally similar (Linde *et al.* 2008). The structural joint approach might be advantageous only where independent geophysical models exhibit at least partial structural similarity, as per the presented examples. In such cases, the additional time needed for tuning the cross-gradient weighting parameter and performing the joint inversion can be justified; conversely, independent inversions can be sufficient to image the main features of the subsurface.

The post-inversion strategy presented in this work for assessing the results of the joint inversion approach is based on a combination of the SCG index and the fuzzy *c*-means clustering. Compared to the unchanged cross-gradients (e.g. Gallardo & Meju 2004, 2007), the SCG index can evaluate changes in structural similarity in the presented models, particularly for highlighting the benefit of the joint approach on the whole model and not only on the main anomaly, whose high magnitude can mask the other contributions. Although able to correctly evaluate the changes (between joint and independent inversions) related to the main anomaly, the unchanged cross-gradient, in fact, fails to properly highlight the benefits of the joint inversion in other areas of the model, where the amplitude of the cross-gradient is often many orders of magnitude weaker (readers may refer to Fig. S1 in Supplementary material). This metric has been calibrated for the parameters under study at the selected sites. Therefore, other choices for

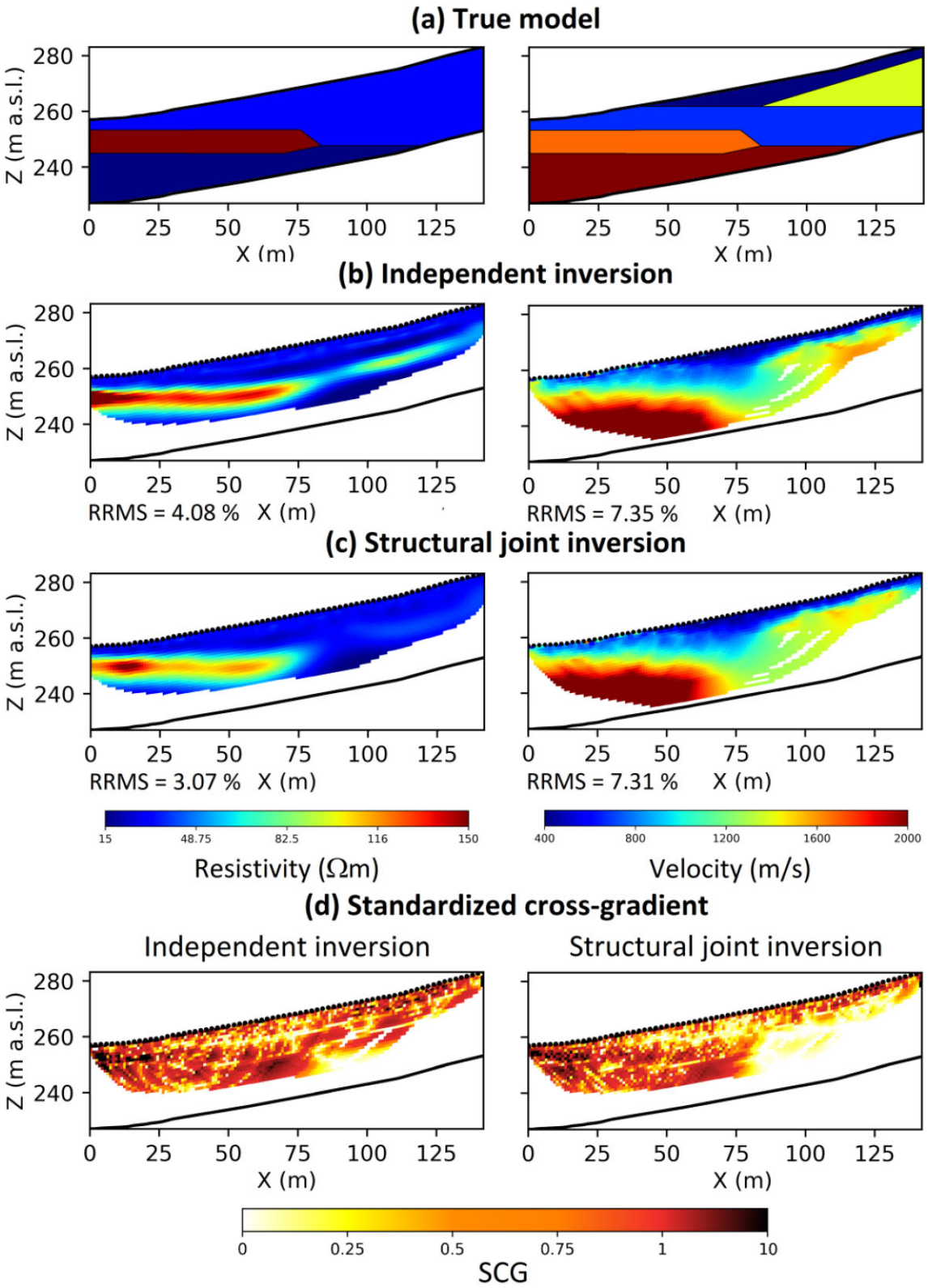

Figure 13. *A-posteriori* synthetic simulation of the Penne dam case study: (a) true model, (b) independent inversion, (c) cross-gradient joint inversion, (d) standardized cross-gradient.

normalizing or standardizing the cross-gradient can be also suitable to enhance the improvement of the joint inversion, but this topic is beyond the scope of this paper and will be investigated thoroughly in future research. Bennington *et al.* (2015) already proposed a normalization of the cross-gradients penalty function, which was incorporated into the joint procedure to remove the dominance of the higher CG values in the near-surface over those at the maximum depths, exceeding 10 km in their investigations. In our applications,

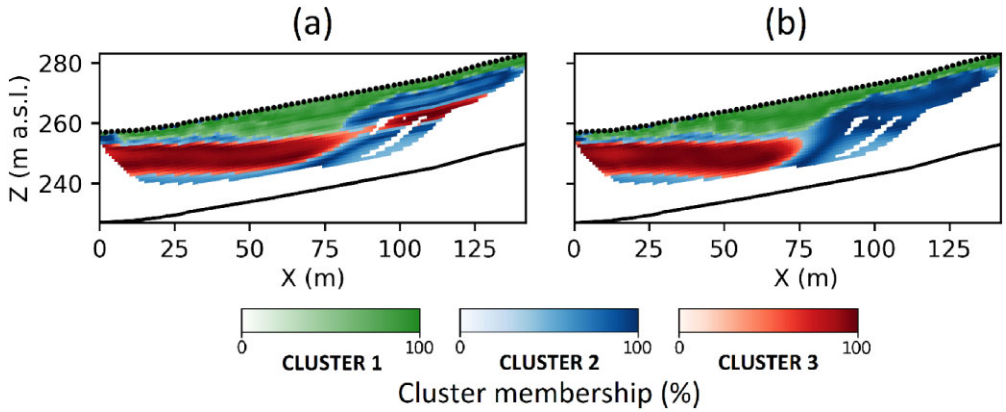

Figure 14. *A-posteriori* synthetic simulation of the Penne dam case study: cluster analysis. (a) Independent inversion, (b) Structural joint inversion.

where the maximum investigation depths are on the order of a few tens of metres similar to Gallardo & Meju (2003, 2004, 2007), the cross-gradients constraint was fully effective during the joint inversion, and we only introduced a statistical reduction of the standard parameter through the computation of the *a-posteriori* SCG index.

Soft clustering algorithms have been rarely applied for a posterior evaluation of the joint inversion approach, even if there are some examples of application of the FCM within the objective function of a joint inversion procedure (e.g. Sun & Li 2016). Other alternatives are a purely qualitative comparison between separate and joint models (e.g. Hamdan & Vafidis 2013; Shi *et al.* 2017; Yari *et al.* 2021), or the isolated use of crisp clustering algorithms (e.g. Hellman *et al.* 2017; Ronczka *et al.* 2017). For the presented three cases, the advantage is twofold: on one hand, we obtained an integrated comparison between independent and joint inverted models information using the clustered sections; on the other hand, the value of the membership function can be a good proxy for assessing of the reliability of the reconstruction. Although a confidence interval for the reconstruction can be achieved only with a stochastic inversion of geophysical data, membership values can be practically interpreted as the probability of a model cell belonging to a geologic unit or anthropogenic features (Sun & Li 2015).

5. CONCLUSIONS

We presented a new algorithm to jointly invert ERT and SRT data on structured mesh incorporating topography using quadrangular elements for preserving the original formulation of the cross-gradient inversion. The benefits of the proposed approach were quantitatively evaluated through a post-inversion procedure in which a new standardization of the cross-gradients assesses the improvement in structural similarity and a fuzzy cluster analysis evaluates the impact in terms of integrated clustered sections. Our approach was applied to a synthetic example and two field cases concerning the investigation of dams through geophysical tomographic techniques. The synthetic example showed the reliability of the proposed algorithm for improving accuracy in model reconstruction in comparison to individual inversions, particularly for the resistivity model and in the low-sensitivity areas or in case of sharp transitions of resistivity and velocity. The application to the real cases confirmed that the advantage of the joint inversion is significant in the low-sensitivity deep zones, close to the interfaces between different layers and in case of abrupt changes of the geophysical properties.

In all cases, the SCG index quantitatively highlights areas where the joint inversion predominantly acts, whereas cluster analysis clearly detected the cluster associated with the desired targets, as validated by the good agreement with synthetic models and boreholes. Therefore, the application of the presented algorithm followed by the proposed post-inversion approach can be highly effective in those problems (e.g. in many civil and environmental engineering applications), where individually inverted models show structural similarity and high accuracy is needed for optimizing the design choices and improving the cost-effectiveness ratio of the whole project.

ACKNOWLEDGMENTS

This research is supported by ‘Sapienza’ University of Rome grant 2021 no. RM12117A8A245367, P.I. Prof. Michele Cercato.

AUTHOR CONTRIBUTIONS

GPdeP: Conceptualization, Data curation, Methodology, Software, Validation, Visualization, Writing—original draft. MC: Investigation, Supervision, Validation, Writing—review and editing. GDD: Investigation, Supervision, Validation, Writing—review and editing.

SUPPORTING INFORMATION

Supplementary data are available at *GJIRAS* online.

Supplementary material_clear.docx

Please note: Oxford University Press is not responsible for the content or functionality of any supporting materials supplied by the authors. Any queries (other than missing material) should be directed to the corresponding author for the paper.

DATA AVAILABILITY

The data sets used in this study are available at the open source repository: https://github.com/Guido-Penta-de-Peppo/Structural-joint-data.

REFERENCES

Bennington, N.L., Zhang, H., Thurber, C.H. & Bedrosian, P.A., 2015. Joint inversion of seismic and magnetotelluric data in the Parkfield region

of California using the normalized cross-gradient constraint, *Pure appl. Geophys.,* **172**(5), 1033–1052.

Bezdek, J.C., 1981. *Pattern Recognition with Fuzzy Objective Function Algorithms,* Plenum Press.

Bièvre, G., Lacroix, P., Oxarango, L., Goutaland, D., Monnot, G. & Fargier, Y., 2017. Integration of geotechnical and geophysical techniques for the characterization of a small earth-filled canal dyke and the localization of water leakage, *J. Appl. Geophys.,* **139,** 1–15.

Cardarelli, E., Cercato, M. & De Donno, G., 2014. Characterization of an earth-filled dam through the combined use of electrical resistivity tomography, P-and SH-wave seismic tomography and surface wave data, *J. Appl. Geophys.,* **106,** 87–95.

Cardarelli, E., Cercato, M. & De Donno, G., 2018. Surface and borehole geophysics for the rehabilitation of a concrete dam (Penne, Central Italy), *Eng. Geol.,* **241,** 1–10.

Constable, S., Parker, R.L. & Constable, C.G., 1987. Occam's inversion; a practical algorithm for generating smooth models from electromagnetic sounding data, *Geophysics,* **52,** 289–300.

Doetsch, J., Linde, N., Coscia, I., Greenhalgh, S.A. & Green, A.G., 2010. Zonation for 3D aquifer characterization based on joint inversions of multimethod crosshole geophysical data, *Geophysics,* **75**(6), 53–64.

Gallardo, L.A. & Meju, M.A., 2003. Characterization of heterogeneous near-surface materials by joint 2D inversion of dc resistivity and seismic data, *Geophys. Res. Lett.,* **30**(13), 1658, doi:10.1029/2003GL017370.

Gallardo, L.A. & Meju, M.A., 2004. Joint two-dimensional DC resistivity and seismic travel time inversion with cross-gradients constraints, *J. Geophys. Res.,* **109**(B3), B03311, doi:10.1029/2003JB002716.

Gallardo, L.A. & Meju, M.A., 2007. Joint two-dimensional cross-gradient imaging of magnetotelluric and seismic traveltime data for structural and lithological classification, *Geophys. J. Int.,* **169**(3), 1261–1272.

Günther, T., Rücker, C. & Spitzer, K., 2006. Three-dimensional modelling and inversion of dc resistivity data incorporating topography—II. Inversion, *Geophys. J. Int.,* **166**(2), 506–517.

Haber, E. & Oldenburg, D.W.,1997. Joint inversion: a structural approach, *Inverse Prob.,* **13,** 63–77.

Hamdan, H.A. & Vafidis, A., 2013. Joint inversion of 2D resistivity and seismic travel time data to image saltwater intrusion over karstic areas, *Environ. Earth Sci.,* **68,** 1877–1885.

Hellman, K., Ronczka, M., Günther, T., Wennermark, M., Rücker, C. & Dahlin, T., 2017. Structurally coupled inversion of ERT and refraction seismic data combined with cluster-based model integration, *J. Appl. Geophys.,* **143,** 169–181.

Jordi, C., Doetsch, J., Günther, T., Schmelzbach, C., Maurer, H. & Robertsson, J.O.A., 2020. Structural joint inversion on irregular meshes, *Geophys. J. Int.,* **220**(3), 1995–2008.

Lelièvre, P.G. & Farquharson, C.G., 2013. Gradient and smoothness regularization operators for geophysical inversion on unstructured meshes, *Geophys. J. Int.,* **195**(1), 330–341.

Linde, N., Binley, A., Tryggvason, A. & Pedersen, L., 2006. Improved hydrogeophysical characterization using joint inversion of crosshole electrical resistance and ground penetrating radar, *Water Resource Res.,* **42**(12), W12404, doi:10.1029/2006WR005131.

Linde, N. & Doetsch, J., 2016. Joint inversion in hydrogeophysics and near-surface geophysics (ch. 7), in *Integrated Imaging of the Earth,* pp. 119–135, eds, Moorkamp, M., Lelievre, P., Linde, N. & Khan, A., Wiley.

Linde, N., Tryggvason, A., Peterson, J. & Hubbard, S., 2008. Joint inversion of crosshole radar and seismic traveltimes acquired at the South Oyster Bacterial Transport Site, *Geophysics,* **73**(4), 29–37.

Linder, S., Paasche, H., Tronicke, J., Niederleithinger, E. & Vienken, T., 2010. Zonal cooperative inversion of crosshole *P*-wave, *S*-wave, and georadar traveltime data sets, *J. Appl. Geophys.,* **72**(4), 254–262.

Marzan, I., Martí, D., Lobo, A., Alcalde, J., Ruiz, M., Alvarez-Marron, J. & Carbonell, R., 2021. Joint interpretation of geophysical data: applying machine learning to the modeling of an evaporitic sequence in Villar de Cañas (Spain), *Eng. Geol.,* **288,** 106126, doi:10.1016/j.enggeo.2021.106126.

Meju, M.A. & Gallardo, L.A.,2016. Structural coupling approaches in integrated geophysical imaging, in *Integrated Imaging of the Earth: Theory and Applications,* pp. 49–67, eds, Moorkamp, M., Lelie`vre, P.G., Linde, N. & Khan, A., Wiley.

Meju, M.A., Gallardo, L.A. & Mohamed, A.K., 2003. Evidence for correlation of electrical resistivity and seismic velocity in heterogeneous near-surface materials, *Geophys. Res. Lett.,* **30**(7), 1373, doi:10.1029/2002GL016048.

Paasche, H., Tronicke, J. & Dietrich, P., 2010. Automated integration of partially colocated models: subsurface zonation using a modified fuzzy c-means cluster analysis algorithm, *Geophysics,* **75**(3), P11–P22.

Paasche, H., Tronicke, J., Holliger, K., Green, A.G. & Maurer, H., 2006. Integration of diverse physical-property models: subsurface zonation and petrophysical parameter estimation based on fuzzy c-means cluster analyses, *Geophysics,* **71**(3), H33–H44.

Ronczka, M., Hellman, K., Günther, T., Wisén, R. & Dahlin, T., 2017. Electric resistivity and seismic refraction tomography: a challenging joint underwater survey at Äspö Hard Rock Laboratory, *Solid Earth,* **8**(3), 671–682.

Rücker, C., Günther, T. & Spitzer, K., 2006. Three-dimensional modeling and inversion of dc resistivity data incorporating topography — I. Modelling, *Geophys. J. Int.,* **166,** 495–505.

Rücker, C., Günther, T. & Wagner, F.M., 2017. pyGIMLi: An open-source library for modelling and inversion in geophysics, *Comput. Geosci.,* **109,** 106–123.

Sasaki, Y., 1989. Two-dimensional joint inversion of magnetotelluric and dipole-dipole resistivity data, *Geophysics,* **54**(2), 254–262.

Shi, Z., Hobbs, R.W., Moorkamp, M., Tian, G. & Jiang, L., 2017. 3-D cross-gradient joint inversion of seismic refraction and DC resistivity data, *J. Appl. Geophys.,* **141,** 54–67.

Sun, J. & Li, Y., 2015. Multidomain petrophysically constrained inversion and geology differentiation using guided fuzzy c-means clustering, *Geophysics,* **80**(4), ID1–ID18.

Sun, J. & Li, Y., 2016. Joint inversion of multiple geophysical data using guided fuzzy c-means clustering, *Geophysics,* **81**(3), ID37–ID57.

Toksöz, M.N., Cheng, C.H. & Timur, A., 1976. Velocities of seismic waves in porous rocks, *Geophysics,* **41**(4), 621–645.

Yari, M., Nabi-Bidhendi, M., Ghanati, R. & Shomali, Z.-H., 2021. Hidden layer imaging using joint inversion of *P*-wave travel-time and electrical resistivity data, *Near Surface Geophys.,* **19,** 297–313.

Zhang, J. & Morgan, F.D., 1996. Joint seismic and electrical tomography, in *Proceedings of EEGS Symposium on Applications of Geophysics to Engineering and Environmental Problems in Keystone,* Colorado, pp. 391–396.